Letter

Metasurface demonstration of exceptional points partitioned by a line of bound states in the continuum

Jiaqi Niu,[1,2] Liyun Zhen,[1,2] Jingquan Liu,[1] and Bin Yang[1,*]

[1]*National Key Laboratory of Advanced Micro and Nano Manufacture Technology, Shanghai Jiao Tong University, Shanghai, 200240, China*

[2]*Department of Micro/Nano Electronics, Shanghai Jiao Tong University, Shanghai, 200240, China*

(Received 17 April 2024; accepted 30 May 2024; published 12 June 2024)

Bound states in the continuum (BICs) and coalesced states at exceptional points (EPs) represent two anomalous resonant states in non-Hermitian systems, attracting extensive interest due to their theoretical implications and practical applications in fields such as sensing, lasing, and nonlinear light-matter interactions. Understanding the relationship between BICs and EPs is therefore of central importance. Recent studies have demonstrated their coexistence in various optical systems, including gratings, photonic crystal slabs, and individual dielectric inclusions. In this paper, we design a simple coupled-split-ring metasurface to demonstrate the connections between BICs and EPs, providing a direct and intuitive mapping of the theoretical predictions from the coupled-mode theory. Specifically, a pair of EPs with opposite chirality is partitioned by a BIC line in the parameter space, indicating that during the process of adiabatic evolution between EPs, one of the modes transitions through a BIC state. Our findings unveil a more comprehensive picture of mode coupling in metasurfaces, paving the way for innovative non-Hermitian system designs and potentially revolutionizing the integration of BICs and EPs within a unified platform for advanced technological applications.

DOI: 10.1103/PhysRevB.109.L241302

In the exploration of quasinormal modes (QNMs) of optical non-Hermitian systems [1,2], which are solutions to source-free Maxwell's equations with appropriate radiation boundary conditions, the modal analysis has spotlighted two extraordinary resonant phenomena [3]: bound states in the continuum (BICs) [4] and exceptional points (EPs) [5]. These phenomena, as special asymptotics of conventional QNMs, reveal the rich complexity of non-Hermitian physics through their unique resonant characteristics—BICs possess real resonant frequencies indicating their nonradiative nature [6,7], whereas EPs are defined by the coalescence of multiple QNMs, leading to identical resonant frequencies and mode profiles under certain parametric conditions [8–10]. In recent years, there have been a burgeoning interest in the study of BICs and EPs, driven by their promising applications in enhancing light-matter interactions, including but not limited to sensing [11,12], lasing [13,14], and the nonlinear control of light [15,16]. Meanwhile, an evolving understanding within the field points towards a unified framework provided by temporal coupled-mode theory (TCMT) [17,18], suggesting a deeper connection between BICs and EPs through the principles of mode coupling [19–21]. This unified perspective has yielded intriguing discoveries on the intricate relations of these two anomalous states [22–28], such as the spawning of EPs from in-Γ BICs within photonic crystal slabs in the momentum space [29] and the proximity of EPs to BICs in various structures, including gratings [30,31] and isolated dielectric particles [21], across various parameter spaces. Although the coexistence of BICs and EPs can be successfully described by the TCMT [19,21], demonstration within the context of metasurfaces remains elusive, despite metasurfaces being a versatile optical platform. In fact, only isolated Friedrich-Wintgen BICs (FWBICs) have been identified [32–34] whereas BIC lines [23,24,35] should also be observed in a two-dimensional parameter space. Additionally, most EPs reported in metasurfaces occur within the polarization space [10,36,37], where the far-field radiations from the uncoupled modes are orthogonal ($\gamma_0 = 0$ in the TCMT as described below), thereby prohibiting the existence of BICs.

In this paper, we design a coupled-split-ring (CSR) metasurface [34] to demonstrate the coexistence of BICs and EPs and investigate their relations. The simple structure of the CSR metasurface allows for a direct and intuitive mapping of the TCMT model, showing semianalytical correlations between the structural parameters and TCMT coefficients. Through QNM calculations, we observe a pair of EPs with opposite chirality that is partitioned by a BIC line in the parameter space. Consequently, one of the QNMs can potentially become a BIC state under the adiabatic evolution between EPs. Our findings provide a comprehensive understanding of the coupling mechanisms in metasurfaces and suggest avenues for the development of advanced non-Hermitian systems, enabling the coherent integration of the distinctive properties of BICs and EPs in a tunable device.

We first delve into FWBICs and EPs in the context of TCMT. This investigation is grounded on a coupling framework between two distinct "base" QNMs, denoted as $|1\rangle$ and $|2\rangle$, as depicted in Fig. 1(a). We model the dynamics of these coupled modes using a two-level effective Hamiltonian $\mathcal{H}$ that captures the behavior of the system within our spectral range of interest, and its matrix representation in the $\{|1\rangle, |2\rangle\}$ basis

*Contact author: binyang@sjtu.edu.cn

 ©2024 American Physical Society

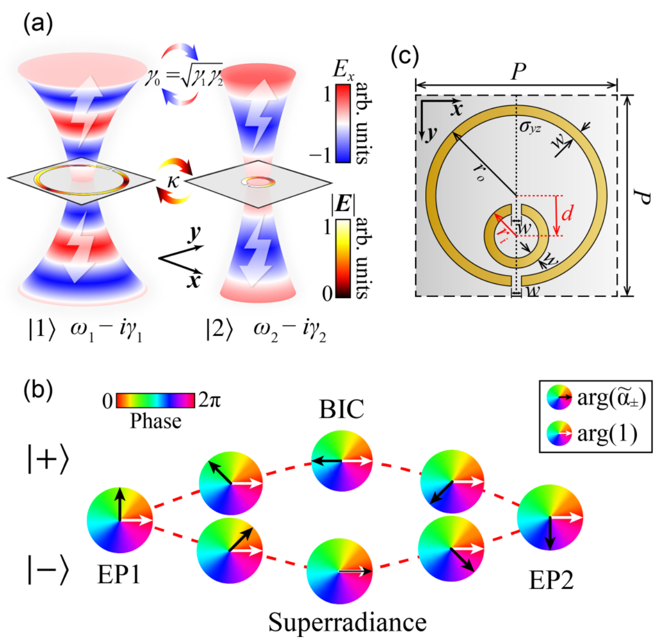

FIG. 1. TCMT model and unit cell of the CSR metasurface. (a) Schematic illustration of the TCMT model with two even modes, $|1\rangle$ and $|2\rangle$, along with the near-field (κ) and far-field ($\gamma_0 = \sqrt{\gamma_1\gamma_2}$) coupling coefficients. Electric field distributions, E_x and $|\boldsymbol{E}|$ show the diverging nature and mode profiles of the two QNMs, respectively. (b) Mode evolution between EPs undergoes a BIC state as $\delta\omega$, $\delta\gamma$, and κ change. The coupling of $|1\rangle$ and $|2\rangle$ results in the "dressed" modes, $|+\rangle$ and $|-\rangle$, see Eq. (5). The black arrows indicate the phase angles of $\tilde{\alpha}_\pm$, where $\arg(\tilde{\alpha}_+) + \arg(\tilde{\alpha}_-) = \pm\pi$. Destructive interference of $|1\rangle$ and $|2\rangle$ is observed at BIC. At EPs, $|+\rangle$ and $|-\rangle$ are coalesced, with $\arg(\tilde{\alpha}_{\mathrm{EP}}) = \pm\pi/2$ signifying distinct chiralities. (c) The unit cell structure of the proposed CSR metasurface, where $P = 300\,\mu\mathrm{m}$, $w = 15\,\mu\mathrm{m}$, $r_o = 135\,\mu\mathrm{m}$. Variable parameters are marked in red.

is described as [17,19,27]

$$\mathcal{H} = \begin{pmatrix} \omega_1 - i\gamma_1 & \kappa - i\gamma_0 \\ \kappa - i\gamma_0 & \omega_2 - i\gamma_2 \end{pmatrix}, \tag{1}$$

where $\tilde{\omega}_{1,2} \equiv \omega_{1,2} - i\gamma_{1,2}$ represent the complex resonant frequencies of $|1\rangle$ and $|2\rangle$. The parameters κ and γ_0 are the near- and far-field coupling coefficients, respectively. It should be noted that $\gamma_0 = \sqrt{\gamma_1\gamma_2}$ is critical to our discussion and is one of the key results derived from TCMT when two base QNMs radiate into the same channel with identical field parity [17]. One the one hand, it is a necessary condition for FWBICs [6,38]; on the other hand, it distinguishes our metasurface in achieving EPs from other designs in which $\gamma_0 \neq \sqrt{\gamma_1\gamma_2}$ due to cross-polarization effects [10,36,37,39]. Note that $\gamma_{1,2} \geqslant 0$ denotes passivity in the system under the convention $\exp(-i\omega t)$, and all scalar variables without a tilde ($\sim$) are real numbers throughout this paper. The eigenvalues of $\mathcal{H}$, $\tilde{\omega}_\pm \equiv \omega_\pm - i\gamma_\pm$, closely approximate the resonant frequencies of the QNMs of the composite system:

$$\tilde{\omega}_\pm = \bar{\omega} - i\bar{\gamma} \pm \sqrt{(\delta\omega - i\delta\gamma)^2 + (\kappa - i\gamma_0)^2}, \tag{2}$$

where $\bar{\omega} \equiv (\omega_1 + \omega_2)/2$, $\bar{\gamma} \equiv (\gamma_1 + \gamma_2)/2$, $\delta\omega \equiv (\omega_2 - \omega_1)/2$ and $\delta\gamma \equiv (\gamma_2 - \gamma_1)/2$. The conditions for BICs and EPs are derived as [19,21,38]:

$$\text{For BICs}: \delta\omega \times \gamma_0 = \delta\gamma \times \kappa \text{ and } \gamma_0 = \sqrt{\gamma_1\gamma_2}, \tag{3}$$

$$\text{For EPs}: \delta\omega = \mp\gamma_0 \text{ and } \kappa = \pm\delta\gamma. \tag{4}$$

The QNMs of the composite system, labeled as $|+\rangle$ and $|-\rangle$, are approximately expressed as superpositions of the base modes $|1\rangle$ and $|2\rangle$, with coefficients derived as eigenvectors of $\mathcal{H}$:

$$|\pm\rangle = -\frac{\delta\tilde{\omega} \pm \sqrt{(\delta\tilde{\omega})^2 + \tilde{\kappa}^2}}{\tilde{\kappa}}|1\rangle + |2\rangle \equiv \tilde{\alpha}_\pm|1\rangle + |2\rangle, \tag{5}$$

where $(\tilde{\alpha}_\pm \quad 1)^T$ correspond to the eigenvectors associated with the eigenvalues $\tilde{\omega}_\pm$, and $\delta\tilde{\omega} \equiv \delta\omega - i\delta\gamma$, $\delta\tilde{\kappa} \equiv \kappa - i\gamma_0$. Although the states $|+\rangle$ and $|-\rangle$ are not normalized in Eq. (5), the emphasis is on the relative contributions of $|1\rangle$ and $|2\rangle$, as represented by the coefficients $\tilde{\alpha}_\pm$. Interestingly, the magnitudes and phases of $\tilde{\alpha}_\pm$ exhibit specific relations:

$$|\tilde{\alpha}_+\tilde{\alpha}_-| = 1, \tag{6}$$

$$\arg(\tilde{\alpha}_+\tilde{\alpha}_-) = \pi. \tag{7}$$

These equations reveal notable interference effects [see Fig. 1(b)]: when $|+\rangle$ represents a BIC, the phase angle of $\tilde{\alpha}_+$, $\arg(\tilde{\alpha}_+)$, equals π, signifying the presence of destructive interference. However, it should be noted that $|\tilde{\alpha}_+| \neq 1$, as will be further elaborated upon in subsequent sections. Conversely, $\arg(\tilde{\alpha}_-) = 0$ suggests that $|-\rangle$ becomes more radiative due to constructive interference. As system parameters vary, two EPs of opposite chirality emerge at $\arg(\tilde{\alpha}_+) = \arg(\tilde{\alpha}_-) = \pm\pi/2$, and concurrently, $|\tilde{\alpha}_+| = |\tilde{\alpha}_-| = 1$. This condition signifies the coalescence of $|+\rangle$ and $|-\rangle$, a requisite characteristic of EPs. Figure 1(b) schematically illustrates the relationships between BICs and EPs, as well as the mode evolutions among different interference states as system parameters shift. Specifically, the diagram shows that in the process of transitioning between EPs through continuous variation of system parameters, one of the modes inevitably passes through a BIC state. Again it should be noted that $\gamma_0 = \sqrt{\gamma_1\gamma_2}$ (an intrinsic property for certain systems as mentioned above) is critical to the formation of BICs; without this condition, the destructive interference is not complete [40]. An overview of the TCMT framework, along with the derivations supporting these results are detailed in Ref. [38].

Aligning with our metasurface design showcased in Fig. 1(c), in which two split-rings (SRs) are integrated within the same plane and embedded in the vacuum, we concentrate on a scenario where the only independent radiation channel consists of linearly polarized plane waves propagating along the $\pm z$ axis. The radiated electric fields are symmetrically distributed (even modes) with respect to the $z = 0$ plane, where the metasurface resides. In contrast to our previous study on the formation of FWBICs [34], in this work, we introduce the variability of both the vertical sliding distance, d, and the outer radius of the inner SR (iSR), r_i (as highlighted in red), to simulate modifications in the coupling coefficient (κ) and the frequency detuning ($\delta\omega$), within the framework of

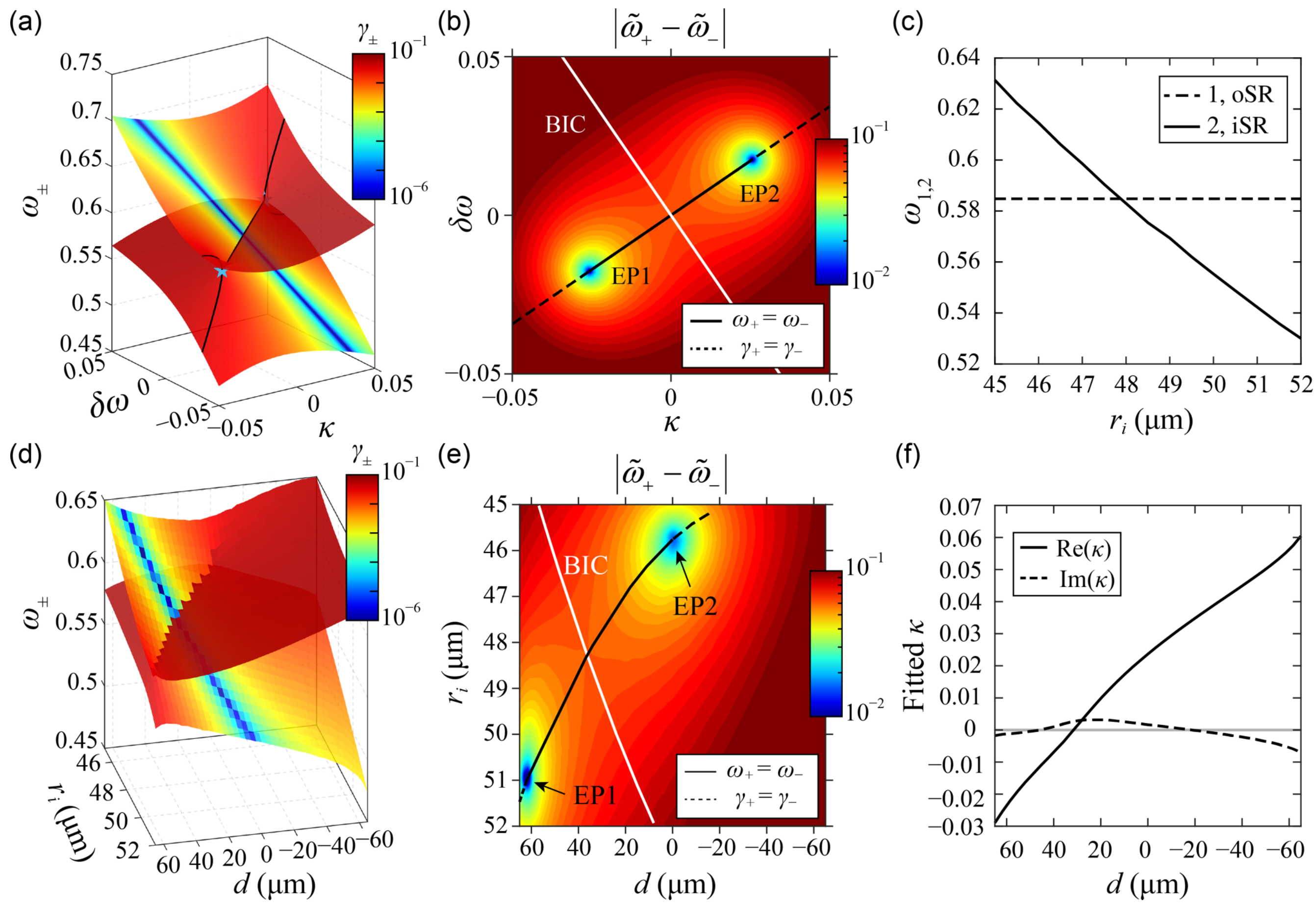

FIG. 2. TCMT predictions of the coexisting BICs and EPs within the $\kappa - \delta\omega$ parameter space and validations using the CSR metasurface within the $d - r_i$ parameter space. (a), (b) Eigenvalues of the effective Hamiltonian $\mathcal{H}$ in the $\kappa - \delta\omega$ space, calculated from the TCMT model [Eq. (2)], where $\gamma_1 = 0.0568$, $\gamma_2 = 0.00546$, and $\omega_1 = 0.585$, all normalized to 1 THz. Two EPs [blue stars in (a)] are separated by a BIC line [white line in (b)]. (c) Resonant frequencies (real part) extracted from simulations of individual SR metasurfaces. The change of r_i mimics the change of $\delta\omega$. (d), (e) Eigenfrequencies of the CSR metasurface in the $d - r_i$ space, similar to (a), (b) but extracted from simulations. (f) Semianalytically fitted near-field coupling coefficient via Eq. (8).

TCMT. The variable d is defined such that the outer SR (oSR) and the iSR are concentric when $d = 0$, with $d > 0$ indicating that the iSR slides along the positive y axis. This setup justifies $\gamma_0 = \sqrt{\gamma_1\gamma_2}$ as specified above, irrespective of d or r_i [17].

An examination of Eqs. (3) and (4) reveals that, within the $\kappa - \delta\omega$ parameter space, BICs delineate a linear trajectory (referred to as the "BIC line") while EPs manifest as isolated points, assuming constant values for γ_1 and γ_2. This setup provides a clear and intuitive framework for analysis, facilitating its straightforward implementation in the design of metasurfaces. Figure 2(a) illustrates this concept by presenting the real ($\omega_\pm$) and imaginary ($\gamma_\pm$) parts of the eigenvalues derived from Eq. (2). A dark blue stripe intersects the "bulk Fermi arc" (where $\omega_+ = \omega_-$) indicating a region of high quality factor [$Q = \omega/(2\gamma)$] adjacent to the BIC line, as specified by Eq. (3). The crossing of the BIC line with the bulk Fermi arc leads to the band exchange effect [23,24,27,31], meaning that BICs transit between the upper and lower bands by crossing the bulk Fermi arc. Additionally, Fig. 2(a) features a so-called "parity-time-symmetry phase transition path" (PTSPT-path) [19], marked by black lines where the band gap closes for either the real or imaginary parts. At two EPs (marked by blue stars), as defined by Eq. (4), the eigenvalues become identical ($\tilde{\omega}_+ = \tilde{\omega}_-$). Such coalescence is more evidently shown in Fig. 2(b). The coefficients used in Figs. 2(a) and 2(b) are detailed in the figure captions. For a more detailed discussion, please refer to Ref. [19], though the primary aim of our study is to validate these theoretical predictions through the design of a practical metasurface. Note that all frequency-related variables have been normalized to 1 THz to facilitate a direct comparison with our metasurface design.

Our simulations were carried out utilizing COMSOL MULTIPHYSICS. The metallic SRs were modeled as lossless structures with perfect electric conductor boundaries. For additional details regarding the simulation, refer to Ref. [38]. Split-rings are known to support multiple resonant modes. For our purpose, we carefully designed the dimensions of both SRs to ensure that the real parts of the resonant frequencies of the quadrupole mode of the oSR (ω_1) and the fundamental mode (LC mode) of the iSR (ω_2) intersect as r_i varies from 45 μm to 52 μm [38]. The near-field electric field distributions ($|\boldsymbol{E}|$) and the correlation between r_i and ω_2 are shown in Fig. 1(a) and Fig. 2(c), respectively. The imaginary part,

γ_2, remains nearly constant but is notably lower than γ_1, as detailed in Ref. [38].

Figures 2(d) and 2(e) present the simulation results for the CSR, serving as counterparts to Figs. 2(a) and 2(b), respectively. All the key features previously mentioned are replicated. Two EPs are identified near $(d, r_i) = (61.8, 50.9)\,\mu\text{m}$ (EP1) and $(d, r_i) = (0, 45.8)\,\mu\text{m}$ (EP2), with a BIC line observable and highlighted by a white line in Fig. 2(e) as a visual guide. Due to the nonlinear dependence between d and κ as well as between r_i and $\delta\omega$, the contour in Fig. 2(e) appears somewhat skewed compared to Fig. 2(b), resulting in the BIC line and the PTSPT path no longer being perpendicular to each other [19].

To establish the connection between the sliding distance (d) and the coupling coefficient (κ), we correlate our simulations with the TCMT model, Eq. (2). To simplify the analysis, we fix $\tilde{\omega}_1$ and $\tilde{\omega}_2$ for each (d, r_i) configuration by referencing Fig. 2(c) and Fig. S3 in Ref. [38]. This approach positions κ as the sole remaining variable to be fitted. Nonetheless, κ is determined through four real equations derived from the parameters $\omega_{1,2}$ and $\gamma_{1,2}$, which effectively leads to its overspecification. However, under the presumption that κ is a function solely of d, we derive a straightforward yet accurate approximation for κ [38]:

$$\kappa = i\gamma_0 \pm \sqrt{\left(\frac{\tilde{\omega}_+ - \tilde{\omega}_-}{2}\right)^2 - (\delta\omega - i\delta\gamma)^2}, \tag{8}$$

opting for the sign that ensures smaller $|\arg(\kappa)|$. The fitted values of κ exhibit nonzero imaginary components due to the approximation techniques used, as depicted in Fig. 2(f). In fact, these imaginary parts can be simply discarded, with the real parts of κ providing a remarkably accurate fit. Remarkably, as the vertical sliding distance d varies, κ spans a broad range of values and notably undergoes a sign switch near $d \approx 33\,\mu\text{m}$, highlighting the unique versatility of our CSR design in modulating coupling dynamics.

With the fitted κ values at hand, we can elucidate the dynamics [shown in Fig. 1(b)] of the CSR metasurface. From Eq. (5), we understand that $\tilde{\alpha}_\pm$ represent the ratios of contributions from $|1\rangle$ and $|2\rangle$ to $|\pm\rangle$. In our context, they can be represented by the ratios of the spatially averaged surface current densities in the x direction for oSR ($\langle\tilde{J}_{S,x}\rangle_{\text{oSR}}$) and iSR ($\langle\tilde{J}_{S,x}\rangle_{\text{iSR}}$), expressed as

$$\tilde{\alpha}_{\pm,\text{sim}} = \frac{\langle\tilde{J}_{S,x}\rangle_{\text{oSR}}}{\langle\tilde{J}_{S,x}\rangle_{\text{iSR}}}, \tag{9}$$

where the spatial average is calculated over the surface of the oSR or iSR within one unit cell, respectively, at the QNMs of the CSR. Due to the out-of-plane (yz) mirror symmetry and the subwavelengthness of the metasurface, the y components are in principle zero [38].

We present comparisons between the TCMT results [shown in dimmed color, Eqs. (5)–(7)] and the simulation results [Eq. (9)] in Figs. 3(a) and 3(b) for two representative r_i values. The red and blue lines represent $|+\rangle$ and $|-\rangle$, respectively, where solid lines denote the amplitudes, and dashed lines denote the phases of $\tilde{\alpha}_\pm$ or $\tilde{\alpha}_{\pm,\text{sim}}$. As analyzed previously in Fig. 1(b), the chirality of the EPs is differentiated by the phases of $\tilde{\alpha}_\pm$. This is confirmed in Figs. 3(a) and 3(b): at EP1, $\arg(\tilde{\alpha}_{\pm,\text{sim}}) \approx \pi/2$ and at EP2 $\arg(\tilde{\alpha}_{\pm,\text{sim}}) \approx -\pi/2$. Moreover, the BIC condition is identified when one of the $\arg(\tilde{\alpha}_{\pm,\text{sim}})$ values equals π, corresponding to a sudden phase jump in the plots due to phase wrapping. More results for generic r_i values are available in [38].

Beyond eigenmode analysis, TCMT enables the prediction of the scattering matrix and the frequency-dependent mode ratio η [see Eq. (11)] [38]. The transmission coefficient, $\tilde{t}$, can be derived as follows:

$$\tilde{t} = 1 + i\frac{(\tilde{\omega}_1 - \omega)\gamma_2 + (\tilde{\omega}_2 - \omega)\gamma_1 - 2\tilde{\kappa}\gamma_0}{(\tilde{\omega}_1 - \omega)(\tilde{\omega}_2 - \omega) - \tilde{\kappa}^2}, \tag{10}$$

and the transmittance, T, is defined as $T \equiv |\tilde{t}|^2$. Incidentally, in the lossless case, it can be shown that $\text{Re}(\tilde{t}) = T$.

Figure 3(c) plots the transmittance at EP2 and the resonant frequencies of the corresponding QNMs, $\tilde{\omega}_\pm$, extracted from both simulation and TCMT for comparison. For more comparisons at generic points on the PTSPT-path, refer to Ref. [38]. Notably, we observe two pronounced resonant features in the transmittance spectrum, although the two underlying QNMs nearly coalesce at an EP. Such spectral features are typically identified as electromagnetically induced transparency (EIT) or the Autler-Townes splitting (ATS) of two modes [41]. However, we argue that the system is, in fact, at an EP, as supported by both TCMT and simulation results. Incidentally, EP is typically considered as the critical point distinguishing between strong and weak coupling [42]; thus in our context it might be served as an alternative threshold to interpret the transmittance spectra as ATS or EIT [41].

The dispersion of the mode ratio η is defined as [38]:

$$\eta(\omega) \equiv \frac{\tilde{a}_1(\omega)}{\tilde{a}_2(\omega)} = \sqrt{\frac{\gamma_1}{\gamma_2}}\frac{\omega - \hat{\omega}_2}{\omega - \hat{\omega}_1}, \tag{11}$$

where $\boldsymbol{a}(\omega) \equiv [\ \tilde{a}_1(\omega) \quad \tilde{a}_2(\omega)\ ]^T$ is the frequency-dependent mode amplitude vector under excitation, with $\hat{\omega}_1 \equiv \omega_1 - \kappa\sqrt{\gamma_1/\gamma_2}$ and $\hat{\omega}_2 \equiv \omega_2 - \kappa\sqrt{\gamma_2/\gamma_1}$. Surprisingly, η is a real number and diverges at $\omega = \hat{\omega}_1$ and vanishes at $\omega = \hat{\omega}_2$. Using the same method for extracting $\tilde{\alpha}_{\pm,\text{sim}}$,

$$\eta_{\text{sim}}(\omega) = \frac{\langle\tilde{J}_{S,x}(\omega)\rangle_{\text{oSR}}}{\langle\tilde{J}_{S,x}(\omega)\rangle_{\text{iSR}}}. \tag{12}$$

Figure 3(d) showcases the theoretical (black) and simulation (red) results, confirming that η_{sim} is real and undergoes a sign change near $\omega = \hat{\omega}_{1,2}$. This suggests that the scattered fields by the oSR and iSR are "phase-locked" and either in-phase or out-of-phase, depending on the excitation frequencies.

Our simple and intuitive CSR metasurface design corroborates the TCMT predictions regarding the coexistence as well as their relations of BICs and EPs within the parameter space. Specifically, a pair of EPs is separated by a BIC line, and therefore, the BIC line intersects the Fermi arc that connects the EPs. While BICs are more abundant than EPs in the parameter space, EPs exhibit greater robustness against loss [38]. The strategic modulation of the frequency detuning $\delta\omega$ and the coupling coefficient κ serves as a universal technique that extends beyond our specific metasurface architecture, proving powerful in uncovering new insights into various physical systems. Notably, the far-field coupling constant (γ_0)

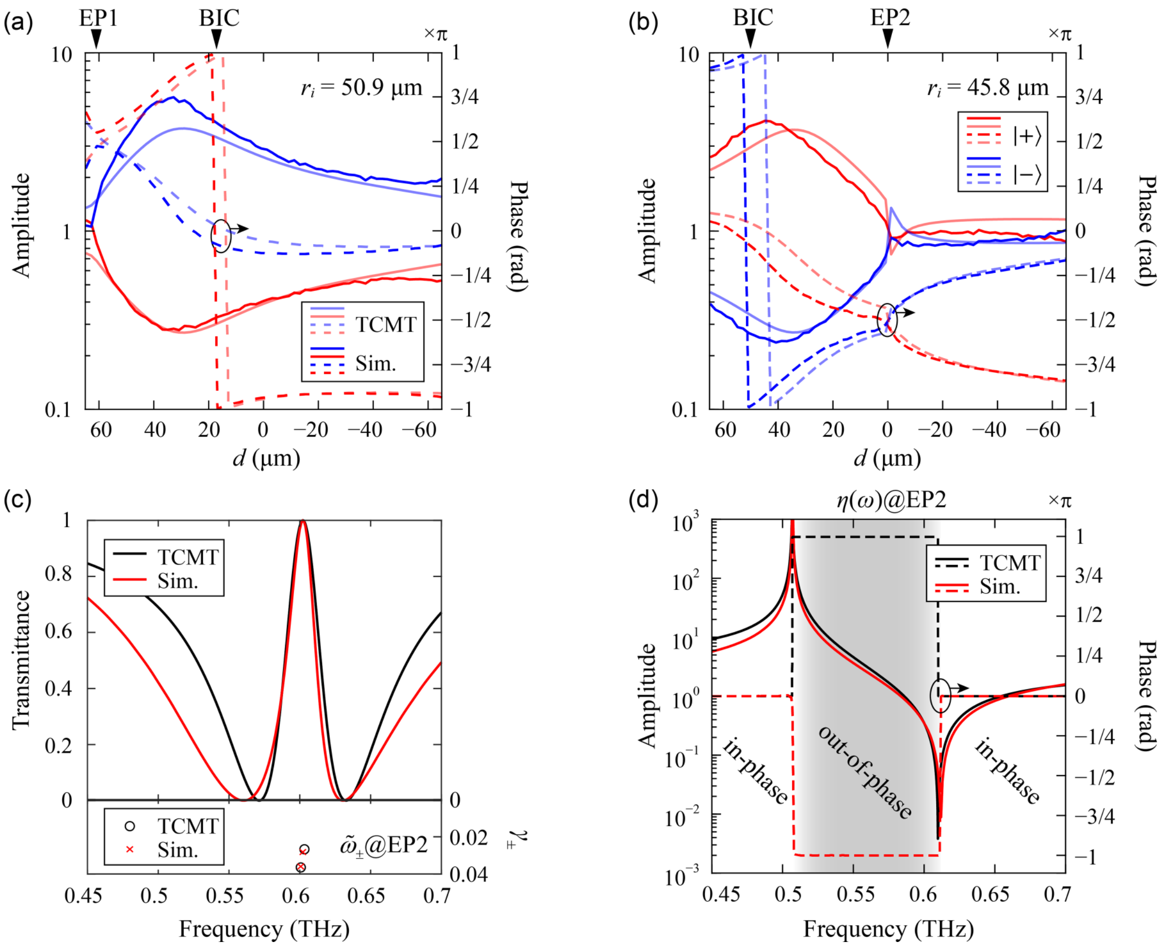

FIG. 3. Curve fittings using previously obtained κ. (a), (b) BIC-EP transition dynamics from the prepesctive of $\tilde{\alpha}_\pm$ [TCMT, dimmed colors, see Eqs. (6) and (7)] and $\tilde{\alpha}_{\pm,\mathrm{sim}}$ [simulation, see Eq. (9)]. The phase jump (dashed lines) at a BIC indicates destructive interference, and the chiralities of EPs are inferred from the phase sign. (c) Transmittanceat EP2. (d) Dispersion of the mode ratio η at EP2. It can be seen from both TCMT and simulation that η is a real number in the lossless case.

plays a pivotal role in our findings, distinguishing our CSR from other designs on the quest for EPs, where γ_0 is typically absent. We also offer a counterintuitive yet enlightening perspective on interpreting the transmittance spectrum through the concept of EPs. Under monochromatic excitation, the phase difference of the constituent base modes is locked at 0 or π, which may find applications in the coherent control of near fields. This study paves the way for further exploration of the nuanced interplay between EPs and BICs, suggesting the promising potential of integrating their unique features into practical designs on a single platform for advanced applications.

This work was supported by the National Natural Science Foundation of China under Grant No. 12072189.

The authors declare no conflicts of interest.

[1] C. Sauvan, T. Wu, R. Zarouf, E. A. Muljarov, and P. Lalanne, Normalization, orthogonality, and completeness of quasinormal modes of open systems: The case of electromagnetism invited, Opt. Express **30**, 6846 (2022).

[2] P. Lalanne, W. Yan, K. Vynck, C. Sauvan, and J.-P. Hugonin, Light interaction with photonic and plasmonic resonances, Laser Photonics Rev. **12**, 1700113 (2018).

[3] W. Yan, P. Lalanne, and M. Qiu, Shape deformation of nanoresonator: A quasinormal-mode Perturbation theory, Phys. Rev. Lett. **125**, 013901 (2020).

[4] S. Neale and E. A. Muljarov, Accidental and symmetry-protected bound states in the continuum in a photonic-crystal slab: A resonant-state expansion study, Phys. Rev. B **103**, 155112 (2021).

[5] H. Zhou, C. Peng, Y. Yoon, C. W. Hsu, K. A. Nelson, L. Fu, J. D. Joannopoulos, M. Soljačić, and B. Zhen, Observation of bulk Fermi arc and polarization half charge from paired exceptional points, Science **359**, 1009 (2018).

[6] C. W. Hsu, B. Zhen, A. D. Stone, J. D. Joannopoulos, and M. Soljačić, Bound states in the continuum, Nat. Rev. Mater. **1**, 465 (2016).

[7] M. V. Rybin, K. L. Koshelev, Z. F. Sadrieva, K. B. Samusev, A. A. Bogdanov, M. F. Limonov, and Y. S. Kivshar, High-Q supercavity modes in subwavelength dielectric resonators, Phys. Rev. Lett. **119**, 243901 (2017).

[8] M.-A. Miri and A. Alù, Exceptional points in optics and photonics, Science **363**, eaar7709 (2019).
[9] E. Bulgakov, K. Pichugin, and A. Sadreev, Exceptional points in a dielectric spheroid, Phys. Rev. A **104**, 053507 (2021).
[10] M. Lawrence, N. Xu, X. Zhang, L. Cong, J. Han, W. Zhang, and S. Zhang, Manifestation of PT symmetry breaking in polarization space with terahertz metasurfaces, Phys. Rev. Lett. **113**, 093901 (2014).
[11] A. Tittl, A. Leitis, M. Liu, F. Yesilkoy, D.-Y. Choi, D. N. Neshev, Y. S. Kivshar, and H. Altug, Imaging-based molecular barcoding with pixelated dielectric metasurfaces, Science **360**, 1105 (2018).
[12] H. Hodaei, A. U. Hassan, S. Wittek, H. Garcia-Gracia, R. El-Ganainy, D. N. Christodoulides, and M. Khajavikhan, Enhanced sensitivity at higher-order exceptional points, Nature (London) **548**, 187 (2017).
[13] A. Kodigala, T. Lepetit, Q. Gu, B. Bahari, Y. Fainman, and B. Kanté, Lasing action from photonic bound states in continuum, Nature (London) **541**, 196 (2017).
[14] B. Peng, Ş. K. Özdemir, M. Liertzer, W. Chen, J. Kramer, H. Yılmaz, J. Wiersig, S. Rotter, and L. Yang, Chiral modes and directional lasing at exceptional points, Proc. Natl Acad. Sci. **113**, 6845 (2016).
[15] K. Koshelev, S. Kruk, E. Melik-Gaykazyan, J.-H. Choi, A. Bogdanov, H.-G. Park, and Y. Kivshar, Subwavelength dielectric resonators for nonlinear nanophotonics, Science **367**, 288 (2020).
[16] V. V. Konotop, J. Yang, and D. A. Zezyulin, Nonlinear waves in PT-symmetric systems, Rev. Mod. Phys. **88**, 035002 (2016).
[17] W. Suh, Z. Wang, and S. Fan, Temporal coupled-mode theory and the presence of non-orthogonal modes in lossless multimode cavities, IEEE J. Quantum Electron. **40**, 1511 (2004).
[18] F. Alpeggiani, N. Parappurath, E. Verhagen, and L. Kuipers, Quasinormal-Mode expansion of the scattering matrix, Phys. Rev. X **7**, 021035 (2017).
[19] Y. Liang, E. Bochkova, S. N. Burokur, A. de Lustrac, H. Benisty, and A. Lupu, Engineering of the Fano resonance spectral response with non-Hermitian metasurfaces by navigating between exceptional point and bound states in the continuum conditions, Opt. Express **32**, 7158 (2024).
[20] A. Krasnok, D. Baranov, H. Li, M.-A. Miri, F. Monticone, and A. Alù, Anomalies in light scattering, Adv. Opt. Photonics **11**, 892 (2019).
[21] N. Solodovchenko, K. Samusev, and M. Limonov, Quadruplets of exceptional points and bound states in the continuum in dielectric rings, Phys. Rev. B **109**, 075131 (2024).
[22] A. C. Valero, Z. Sztranyovszky, E. A. Muljarov, A. Bogdanov, and T. Weiss, Exceptional bound states in the continuum, arXiv:2309.01501.
[23] P. Pujol-Closa and D. Artigas, Dirac points embedded in the continuum, Phys. Rev. B **108**, 205106 (2023).
[24] A. Cerjan, C. W. Hsu, and M. C. Rechtsman, Bound states in the continuum through environmental design, Phys. Rev. Lett. **123**, 023902 (2019).
[25] H. Qin, X. Shi, and H. Ou, Exceptional points at bound states in the continuum in photonic integrated circuits, Nanophotonics **11**, 4909 (2022).
[26] Q. Song, J. Hu, S. Dai, C. Zheng, D. Han, J. Zi, Z. Q. Zhang, and C. T. Chan, Coexistence of a new type of bound state in the continuum and a lasing threshold mode induced by PT symmetry, Sci. Adv. **6**, eabc1160 (2020).
[27] X. Yin, T. Inoue, C. Peng, and S. Noda, Topological unidirectional guided resonances emerged from interband Coupling, Phys. Rev. Lett. **130**, 056401 (2023).
[28] S.-G. Lee, S.-H. Kim, and C.-S. Kee, Band dynamics accompanied by bound states in the continuum at the third-order Γ point in leaky-mode photonic lattices, Photonics Res. **9**, 1109 (2021).
[29] M. Kang, W. Zhu, H.-T. Wang, and M. Premaratne, Spawning a ring of exceptional points from a metamaterial, Opt. Express **25**, 18265 (2017).
[30] G. Shadrina, E. Bulgakov, A. Sadreev, and K. Pichugin, Exceptional points in periodic array of silicon rods, Appl. Phys. Lett. **123**, 211104 (2023).
[31] R. Kikkawa, M. Nishida, and Y. Kadoya, Bound states in the continuum and exceptional points in dielectric waveguide equipped with a metal grating, New J. Phys. **22**, 73029 (2020).
[32] X. Zhao, C. Chen, K. Kaj, I. Hammock, Y. Huang, R. D. Averitt, and X. Zhang, Terahertz investigation of bound states in the continuum of metallic metasurfaces, Optica **7**, 1548 (2020).
[33] H. Friedrich and D. Wintgen, Interfering resonances and bound states in the continuum, Phys. Rev. A **32**, 3231 (1985).
[34] J. Niu, Y. Zhai, Q. Han, J. Liu, and B. Yang, Resonance-trapped bound states in the continuum in metallic THz metasurfaces, Opt. Lett. **46**, 162 (2021).
[35] J. Gomis-Bresco, D. Artigas, and L. Torner, Anisotropy-induced photonic bound states in the continuum, Nat. Photon. **11**, 232 (2017).
[36] Q. Song, M. Odeh, J. Zúñiga-Pérez, B. Kanté, and P. Genevet, Plasmonic topological metasurface by encircling an exceptional point, Science **373**, 1133 (2021).
[37] M. Kang, J. Chen, and Y. D. Chong, Chiral exceptional points in metasurfaces, Phys. Rev. A **94**, 033834 (2016).
[38] See Supplemental Material at http://link.aps.org/supplemental/10.1103/PhysRevB.109.L241302 for an overview of the TCMT framework, simulation details, curve fitting details and discussions on the loss effects, which includes Refs. [1,6,17–19,41,42].
[39] C. Li, R. Yang, X. Huang, Q. Fu, Y. Fan, and F. Zhang, Experimental demonstration of controllable PT and anti-PT coupling in a non-Hermitian metamaterial, Phys. Rev. Lett. **132**, 156601 (2024).
[40] Y. Jian, Y. Wang, Z. Guo, S. Hu, B. Wu, Y. Yang, and H. Chen, External excitation enabled chirality reversal of exceptional points in an effective anti-PT-symmetric non-Hermitian system, Appl. Phys. Lett. **123**, 141702 (2023).
[41] B. Peng, S. K. Özdemir, W. Chen, F. Nori, and L. Yang, What is and what is not electromagnetically induced transparency in whispering-gallery microcavities, Nat. Commun. **5**, 5082 (2014).
[42] S. R.-K. Rodriguez, Classical and quantum distinctions between weak and strong coupling, Eur. J. Phys. **37**, 25802 (2016).